

Field-tunable toroidal moment and anomalous Hall effect in noncollinear antiferromagnetic Weyl semimetal $\text{Co}_{1/3}\text{TaS}_2$

Pyeongjae Park^{1,2}, Yoon-Gu Kang³, Junghyun Kim^{1,2}, Ki Hoon Lee⁴, Han-Jin Noh⁵, Myung Joon Han^{3*}, and Je-Geun Park^{1,2,6*}

¹*Center for Quantum Materials, Seoul National University, Seoul 08826, Republic of Korea*

²*Department of Physics & Astronomy, Seoul National University, Seoul 08826, Republic of Korea*

³*Department of Physics, KAIST, Daejeon 34141, Republic of Korea*

⁴*Department of Physics, Incheon National University, Incheon, 22012, Republic of Korea*

⁵*Department of Physics, Chonnam National University, Gwangju 61186, Republic of Korea*

⁶*Institute of Applied Physics, Seoul National University, Seoul 08826, Republic of Korea*

* Corresponding author: jgpark10@snu.ac.kr & mj.han@kaist.ac.kr

Abstract

Combining magnetism with band topology provides various novel phases that are otherwise impossible. Among several cases, noncollinear metallic antiferromagnets can reveal particularly rich topological physics due to their diverse magnetic ground states. However, there are only a few experimental studies due to the lack of suitable materials, especially with triangular lattice antiferromagnets. Here, we report that metallic triangular antiferromagnet $\text{Co}_{1/3}\text{TaS}_2$ exhibits a substantial anomalous Hall effect (AHE) related to its noncollinear magnetic order. Our first-principles calculations found that hourglass Weyl fermions from the non-symmorphic symmetry trigger AHE. We further show that AHE in $\text{Co}_{1/3}\text{TaS}_2$ can be characterized by the *toroidal moment*, a vortex-like multipole component that arises from a combination of chiral lattice and geometrical frustration. Finally, the unusual field-tunability of the toroidal moment puts $\text{Co}_{1/3}\text{TaS}_2$ as a rare example of a noncollinear metallic antiferromagnet filled with interesting magnetic and topological properties.

Introduction

Introducing magnetic order into electron band structure presents an exciting opportunity to realize topological phases otherwise unavailable in non-magnetic systems. Such phases can emerge from perturbations due to magnetism on the electronic band structure's geometry and topology. Anomalous Hall effect (AHE) in metallic ferromagnets is the most direct consequence of such perturbations. However, the more interesting case of magnetic topological band structure lies with antiferromagnets, which provide several interesting situations and could, in principle, offer unseen properties arising simply from the enormous number of possible spin configurations^{1,2}. One of the most remarkable properties is the sizable AHE in a metallic antiferromagnet despite its zero or vanishingly small net magnetization, which is roughly proportional to AHE in the case of ferromagnets. Thus, a different organizing principle than magnetization on its own should govern the AHE in antiferromagnets.

To understand AHE in metallic antiferromagnets, one should identify an effective order parameter that characterizes the symmetry-breaking field that leads to finite AHE. One example is AHE from non-coplanar magnetic order (also known as topological Hall effect), which can be well characterized by scalar spin chirality^{3,4}. More interestingly, it has been recently suggested that noncollinear antiferromagnets with coplanar magnetic order can also manifest a large AHE with the aid of spin-orbit coupling⁵⁻⁹. In this case, AHE can be characterized by the cluster multipole moment^{10,11}. Despite such an exciting organizing principle, however, there are still no relevant experimental results except for the only one known example of such: that is, the cluster octupole moments in Mn_3X ($X=Ge, Sn, Ir$)^{1,2,10-12}. In other words, the richness of noncollinear antiferromagnetic configuration space with non-trivial band structure is just a hypothetical proposition at the moment. Hence, finding another noncollinear antiferromagnet is the crucial way forward to materialize the untapped potential of antiferromagnetic metallic systems, which would give access to AHE originating from a much more diverse multipole magnetism, where unique physics may be found in each case. This may, in particular, hold for a multipole called toroidal moment. Because it requires breaking both

space inversion and time-reversal symmetry (TRS), the ordering of toroidal moments (i.e., ferrotoroidal order) is distinct from that of magnetic multipoles¹³ and therefore can manifest some non-trivial phenomena. However, due to the scarcity of suitable materials, relatively less attention has been paid to this multipole class so far, which prevents a complete understanding of its connection to macroscopic quantities measured by experiments.

$\text{TM}_{1/3}\text{MS}_2$ (TM=3d transition metals and M=Ta, Nb) are promising materials for studying metallic antiferromagnetism in a triangular lattice^{14,15}. It consists of well-known metallic $2H\text{-MS}_2$ with triangular layers of TMs intercalating into a vdW gap of $2H\text{-MS}_2$ (Fig. 1a). Such intercalation slightly alters the atomic positions of sulfur atoms, leading to the chiral structure with a non-centrosymmetric $P6_322$ space group (No. 182)¹⁶. The charge transfer from TM to $2H\text{-MS}_2$ forms divalent (TM^{2+}) or trivalent (TM^{3+}) TM ions, and subsequently localized magnetic moments settle down in TM sites (Fig. 1b). Interestingly, this material class exhibits various magnetic ground states depending on the choice of TM and M¹⁴. Among the combinations, $\text{Co}_{1/3}\text{TaS}_2$ is the only material with the noncollinear 120° magnetic order¹⁷, a natural outcome due to geometrical frustration (Fig. 1b). Therefore, $\text{Co}_{1/3}\text{TaS}_2$ offers a combination of chirality, triangular lattice, and 120° magnetic structure, unique among the current set of magnetic topological materials. Moreover, $\text{TM}_{1/3}\text{MS}_2$ can be thinned down to a few atomic layers through mechanical exfoliation¹⁸. Hence, it could also open up an entirely new route to study noncollinear antiferromagnetism and corresponding topological physics in genuine two-dimension.

This work reports that single-crystal $\text{Co}_{1/3}\text{TaS}_2$ is a metallic triangular antiferromagnet where coplanar 120° magnetic order plays a crucial role in forming electron band topology and concomitant AHE. Our density functional theory (DFT) calculations show that AHE is triggered by hourglass Weyl

fermions enforced by non-symmorphic symmetry under broken TRS. Moreover, we explain how the toroidal moment, a multipole component in non-centrosymmetric chiral antiferromagnets¹³, can characterize AHE in $\text{Co}_{1/3}\text{TaS}_2$. Finally, we discuss the remarkable tunability of the toroidal moment under an out-of-plane magnetic field, which implies a profound correlation between AHE and the magnetism of $\text{Co}_{1/3}\text{TaS}_2$.

Results and Discussion

Bulk properties Temperature-dependent magnetization (\mathbf{M}), resistivity (ρ_{xx}), and specific heat (C_p) of $\text{Co}_{1/3}\text{TaS}_2$ indicate two magnetic phase transitions at $T_{N1}=38$ K and $T_{N2}=26.5$ K (Fig. 1c-f). The major transition occurs at T_{N2} , where all the properties change significantly. The negative Curie-Weiss temperature (θ_{CW}) with a significant frustration factor $f \equiv \frac{|\theta_{CW}|}{T_{N2}} \sim 4$ indicates dominant antiferromagnetic interactions with frustration, consistent with the formation of the 120° order. Interestingly, the phase below T_{N2} involves a weak ferromagnetic moment of $0.01 \mu_B/\text{Co}^{2+}$ along the c-axis ($M_z(\mathbf{H} = 0)$), as shown in the field dependence of M_z with hysteresis (Fig. 1d). In addition to the domain switch of $M_z(\mathbf{H} = 0)$ at $\pm H_{c1}$, there is a jump at $\pm H_{c2}$ due to a meta-magnetic transition. The mechanism of this meta-magnetic transition remains unclear due to limited information, which requires further studies.

Most interestingly, the AHE ($\rho_{xy}(\mathbf{H} = 0)$) appears below T_{N2} , despite the antiferromagnetic nature of $\text{Co}_{1/3}\text{TaS}_2$ (Fig. 2a). The anomalous Hall conductivity (AHC, $\sigma_{xy}(\mathbf{H} = 0)$) reaches a value of $70 \Omega^{-1}\text{cm}^{-1}$ at 2 K, comparable to those measured in ferromagnetic materials³. After excluding the linear Hall effect, the magnitude of the $\rho_{xy}(\mathbf{H})$ remains nearly unchanged with varying a magnetic field, except for a jump at H_{c2} . Also, the observed hysteresis of AHE with a significant coercive field H_{c1} is quite similar to that of the weak ferromagnetic moment (Fig. 2b), particularly in that they

simultaneously flip to the opposite domain. This connection between the two quantities shall be discussed later in this paper.

The shape of the hysteresis itself is interesting and merits separate comments. First of all, the meta-magnetic transition at $\pm H_{c2}$ already starts to appear when $T_{N2} < T < T_{N1}$ (Supplementary Figure 5), indicating that the meta-magnetic transition is more related to the magnetic order corresponding to T_{N1} . Second, the domain switch at H_{c1} and the meta-magnetic transition at H_{c2} are not independent. While H_{c2} remains nearly unchanged, H_{c1} increases rapidly with decreasing temperature from T_{N2} and reaches almost 9 T at 2 K (Fig. 2c). Indeed, the crossover between H_{c1} and H_{c2} should occur somewhere below T_{N2} , around 14 K (Fig. 2c). Surprisingly, the domain switch and the meta-magnetic transition happen simultaneously at H_{c1} after the crossover ($|H_{c1}| > |H_{c2}|$), resulting in a peculiar shape of hysteresis below 15 K (Fig. 2a-b). Thus, the two-fold magnetic domain with respect to the c-axis, the metamagnetic transition at $\pm H_{c2}$, and the magnetic order that forms at T_{N1} and T_{N2} are deeply related to each other, which requires further studies for a complete understanding.

Moreover, the temperature evolution of $\sigma_{xy}(\mathbf{H} = 0)$ in $\text{Co}_{1/3}\text{TaS}_2$ behaves just like an order parameter of the phase transition at T_{N2} (Fig. 2d), implying that the observed AHE is closely related to the magnetic order of $\text{Co}_{1/3}\text{TaS}_2$. This hypothesis is further supported by the fact that the critical exponent β of $\sigma_{xy}(T, \mathbf{H} = 0)$ is nearly identical to that of $M_z(T, \mathbf{H} = 0)$, as shown in Fig. 2e. Note that the fitted β is close to 0.5, consistent with the fact that the magnetic order mediated by long-ranged RKKY interaction follows the mean-field critical behavior¹⁹. Finally, we compared the magnitude of $\sigma_{xy}(\mathbf{H} = 0)$ measured below 15 K for several samples with different Co compositions ($0.310 < x < 0.325$). While ρ_{xx} and ρ_{xy} vary depending on the samples, $\sigma_{xy}(\mathbf{H} = 0)$ and the shape of the hysteresis remain nearly the same for all the samples (Fig. 2f and Supplementary Figure 6).

Theoretical understanding of AHE The observed AHC's robustness and its close connection to the magnetic order imply the intrinsic nature of the AHE in $\text{Co}_{1/3}\text{TaS}_2$. The following two possibilities are not likely the situation of $\text{Co}_{1/3}\text{TaS}_2$, based on our findings regarding its microscopic relation to the magnetic order. First, although $\text{Co}_{1/3}\text{TaS}_2$ has a small weak ferromagnetic moment, the observed AHE in $\text{Co}_{1/3}\text{TaS}_2$ cannot be totally attributed to the weak ferromagnetic moment itself. This is because the field evolution of AHE does not match with that of M_z ; see dM_z/dH and $d\rho_{xy}/dH$ at H_{c1} and H_{c2} . Also, $M_z(\mathbf{H} = 0) \sim 0.01 \mu_B/\text{Co}^{2+}$ itself is too small to induce $\sigma_{xy}(\mathbf{H} = 0)$ as large as $\sim 70 \Omega^{-1}\text{cm}^{-1}$. Nor could it originate from the scalar spin chirality due to the slight out-of-plane canting, as the spin chirality is usually canceled out in a triangular lattice antiferromagnet with 120° order²⁰. Therefore, understanding AHE in $\text{Co}_{1/3}\text{TaS}_2$ requires a new idea related to the coplanar 120° spin order itself, analogous to the case in noncollinear kagome antiferromagnet Mn_3X ($\text{X}=\text{Ge}, \text{Sn}$)^{5,7}.

We first begin with symmetry arguments for the possible 120° magnetic order in $\text{Co}_{1/3}\text{TaS}_2$, which can formulate the existence of AHE. According to the group-theoretical analysis²¹, the possible magnetic ground states can be described by six irreducible representations referred to as $\Gamma_1 \sim \Gamma_6$ (Supplementary Figure 8). Note that Γ_1 , Γ_2 , and Γ_5 spin configurations can be transformed into each other through uniform spin rotation around the c-axis (θ in Fig. 3a). Notably, the two-fold rotation (C_{2a} or C_{2a^*}) and the 6_3 screw symmetry combined with time-reversal ($\equiv \underline{6}_3$) forbid finite $\sigma_{xy}(\mathbf{H} = 0)$ and $M_z(\mathbf{H} = 0)$ in $\text{Co}_{1/3}\text{TaS}_2$: e.g., Γ_1 ($P6_322$) in Fig. 3a (for more explanation, see Supplementary Text). Consequently, only Γ_2 ($P6_3\underline{22}$) and the Γ_5 ($P6_3$) can possess finite $\sigma_{xy}(\mathbf{H} = 0)$ and $M_z(\mathbf{H} = 0)$ and explain our experimental results. Yet Γ_5 is a two-dimensional irreducible representation with much lower symmetry, and therefore, is less likely to occur in natural materials, as pointed out in previous studies of two-dimensional triangular antiferromagnets²². Thus, we focus on the Γ_2 spin configuration in our analysis (Fig. 3b and 3c). Our data indeed support such a choice

as magnetic susceptibility measured along the a-axis is slightly larger than that along the a^* -axis (Fig. 1c); aligning the spins along the a-axis or its symmetrically equivalent directions is energetically more favorable (i.e., local easy-axes), which is the case of Γ_2 as shown in Fig. 3b. Also, as shown in Fig. 3d, the total energy obtained from our DFT calculation reaches its minimum when $\theta=0^\circ$ ($=\Gamma_2^+$) or 180° ($=\Gamma_2^-$), which is another evidence supporting the Γ_2 ground state.

The observed intrinsic AHE can be understood as a manifestation of novel Weyl fermions in the electron band structure of $\text{Co}_{1/3}\text{TaS}_2$, where non-symmorphic symmetry enforces their existence. Notably, the crystal structure of $\text{Co}_{1/3}\text{TaS}_2$ has the 6_3 screw symmetry that remains unbroken in the Γ_2 representation. Such non-symmorphic symmetry could result in specific Weyl crossings in the \mathbf{k} -space called hourglass Weyl fermion²³⁻²⁵. Fig. 4a shows the schematic band dispersion representing a typical situation of hourglass Weyl fermions. Along the screw-invariant line connecting time-reversal invariant momenta (TRIM) points (say, $\Gamma - A$ and $M - L$), there must be band crossings as guaranteed by screw symmetry. By half-translation, the eigenstates of the 2_1 screw symmetry operation acquire a momentum-dependent phase factor of $e^{-ik_z c/2}$ (c is the lattice constant along the c-axis), and it then causes Kramers' pair exchange (indicated by using color code) as k_z moves from one TRIM point to another. Consequently, the pairs of bands must cross at least once within the invariant space, which naturally makes the band dispersion have the 'hourglass' shape and creates inevitable Weyl crossing (olive circles in Fig. 4a).

To confirm this scenario for $\text{Co}_{1/3}\text{TaS}_2$, we carried out DFT calculations with the Γ_2 spin configuration (Fig. 4b): we also tested other possible spin configurations with less promising results. As marked in color, certain pockets of the \mathbf{k} -space contain the anticipated novel hourglass type dispersion enforced by the 6_3 screw symmetry. It is especially notable that, protected by the screw symmetry, the Weyl 'crossing' point in the hourglass dispersion can be preserved even under TRS

breaking²⁶. Fig. 4c and 4d show the enlarged band dispersion along the $\overline{\Gamma\text{A}}$ and $\overline{\text{M}\text{L}}$ lines using the Γ_2 spin configuration (Fig. 4b), where the color scale indicates the 2_1 screw rotation eigenvalues. Due to the absence of TRS, Γ , A, M, and L are no longer TRIM points (Fig. 4c and 4d). Thus, the Kramers' degeneracies are lifted at these points (indicated by gray arrows in Fig. 4d), although the degeneracy lifting is not visible at the Γ and A points in this energy scale. However, the hourglass dispersion and the Weyl crossings (the olive circles in Fig. 4c and 4d) are still well maintained. This is clearly shown when comparing Fig. 4c and 4d with Fig. 4a; the evolution of the screw operation's eigenvalue is essentially the same as each other. We note that few theoretical studies have shown the hourglass Weyl fermions with broken TRS, which adopted simple ferromagnetic or collinear antiferromagnetic spin order²⁷⁻²⁹.

From the AHC's point of view, however, the Weyl crossings along the $\overline{\Gamma\text{A}}$ and $\overline{\text{M}\text{L}}$ lines, albeit interesting, cannot be responsible for the observed AHE. It is simply because their locations are too far off from the Fermi level (see Fig. 4b). Instead, we found that the Weyl points on the $\overline{\text{K}\text{H}}$ line play a more critical role. Although both K and H points are not the TRIM points even with TRS, the existence of Weyl points on the $\overline{\text{K}\text{H}}$ line is guaranteed by the hourglass Weyl points on the $\overline{\Gamma\text{A}}$ and $\overline{\text{M}\text{L}}$ lines due to the fermion doubling theorem^{30,31}. From the fact that Weyl points on the $\overline{\Gamma\text{A}}$ and $\overline{\text{M}\text{L}}$ line respectively have a multiplicity of 1 and 3 in half Brillouin zone (BZ), Weyl points are required to lie also on the $\overline{\text{K}\text{H}}$ line with a multiplicity of 2 to neutralize the chiral charge: $\nu_{\Gamma\text{A}} + 3\nu_{\text{M}\text{L}} + 2\nu_{\text{K}\text{H}} = 0$. As displayed in Fig. 4e, there are indeed multiple Weyl crossings along the $\overline{\text{K}\text{H}}$ line, generating Berry curvature like a magnetic monopole. Moreover, since they are located close enough to the Fermi level, they are likely to make a dominant contribution to the anomalous charge transport. The results presented in Fig. 4f constitute more convincing evidence supporting our argument. The black and orange line represents the calculated AHC obtained by integrating the whole BZ and only along the $\overline{\text{K}\text{H}}$ line, using several 120° spin configurations specified by θ in Fig. 3a, i.e., using Γ_1 ($\theta = 90^\circ$ or 270°), Γ_2 ($\theta = 0^\circ$ or 180°), and Γ_5 (other angles) spin configurations. First, the

calculated $|\sigma_{xy}|$ using the Γ_2 configuration is about $90 \Omega^{-1}\text{cm}^{-1}$, which is indeed in excellent agreement with our experimental results (Fig. 2d and 2f). Also, only a small difference is found between the σ_{xy} calculated over the entire BZ and that obtained only along the $\overline{\text{KH}}$ line, implying that the most dominant contribution of σ_{xy} comes from the Weyl points in this particular $\overline{\text{KH}}$ symmetry line. Taken together, the ‘vestige’ of hourglass Weyl fermions on the $\overline{\Gamma\text{A}}$ and $\overline{\text{ML}}$ lines, which remains intact under the 120° magnetic order, triggers the AHE in this material despite the broken TRS and the lifted degeneracy otherwise residing at Γ , A, M, and L.

AHE and toroidal moment Fig. 4f further demonstrates that the AHC strongly depends on the detailed in-plane spin configuration of $\text{Co}_{1/3}\text{TaS}_2$. To put it intuitively, a vortex-like arrangement inside the 120° spin configuration breaks the C_{2a} or C_{2a^*} symmetry and allows finite $\sigma_{xy}(\mathbf{H} = 0)$ in $\text{Co}_{1/3}\text{TaS}_2$. Fig. 3a and 3b show two clear cases: one is without the vortex-like arrangement of Γ_1 and another is with the vortex-like arrangement of Γ_2 . Such an arrangement can be precisely quantified by the toroidal dipole moment (\mathbf{t})^{11,13,32}:

$$\mathbf{t} \equiv \sum_i \mathbf{r}_i \times \mathbf{S}_i \quad (1)$$

where \mathbf{r}_i is the position vector of the i^{th} site from the center of the six Co atoms with hexagonal configuration (Fig. 3b). Unlike ordinary magnetic or electric multipoles, \mathbf{t} breaks both inversion and time-reversal symmetry and consequently appears in a non-centrosymmetric chiral magnet with geometrical frustration^{13,32}. Therefore, $\text{Co}_{1/3}\text{TaS}_2$ is a rare system that can have non-zero \mathbf{t} , and so it is helpful for a proper understanding of its role in characterizing AHE, which has been suggested only in theory so far¹¹. Fig. 3e shows a complete comparison between t_z and calculated σ_{xy} for the Γ_1 , Γ_2 , and Γ_5 spin configurations. As expected, it clearly reveals the aspect of t_z as the order parameter characterizing the AHE.

From this point of view, we can interpret the Γ_2^+ ($\theta = 0^\circ$) and Γ_2^- ($\theta = 180^\circ$) spin configurations as a pair of ferro-toroidal states with an opposite sign of t_z (Fig. 3b and 3c). Interestingly enough, the sign change of σ_{xy} at $\pm H_{c1}$ then corresponds to the transition between the Γ_2^+ and the Γ_2^- configurations (Fig. 3f). In other words, an out-of-plane magnetic field switches the AHE of $\text{Co}_{1/3}\text{TaS}_2$ by manipulating the in-plane spin configuration. While such a consequence may appear at first sight somewhat surprising, it is the weak ferromagnetic moment that connects the out-of-plane field and the in-plane spin configuration in $\text{Co}_{1/3}\text{TaS}_2$. The simultaneous jump of σ_{xy} and M_z seen in our experiments (Fig. 2a and 2b) implies that the sign of t_z is coupled to the sign of $M_z(\mathbf{H} = 0)$; i.e., the Γ_2^+ (Γ_2^-) configuration always tends to have positive (negative) $M_z(\mathbf{H} = 0)$. Consequently, the out-of-plane magnetic field can effectively control the sign of t_z by flipping $M_z(\mathbf{H} = 0)$, consistent with the similar hysteretic behavior of σ_{xy} to that of M_z (see Fig. 2a and 2b). The coexistence of the toroidal moment and the weak ferromagnetic moment in $\text{Co}_{1/3}\text{TaS}_2$ is not accidental. A combination of lattice chirality and toroidal spin configuration results in the broken two-fold rotation (C_{2a}, C_{2a^*}), mirror, and TRS. Such a situation leads to the emergence of a finite vector quantity along the chiral axis (the c-axis in $\text{Co}_{1/3}\text{TaS}_2$), whose transformation property is equivalent to that of magnetization^{33,34}. Of further interest, t_z can be coupled to $M_z(\mathbf{H} = 0)$ at the microscopic level, where a symmetry-allowed higher-order on-site anisotropy can clearly describe such a property in $\text{Co}_{1/3}\text{TaS}_2$ (see Supplementary Text and Supplementary Figure 11).

We finally note that a two-fold crystallographic chiral domain related to left or right-handedness, which itself is another interesting topic in $\text{TM}_{1/3}\text{MS}_2$ (Ref. ^{35,36}), is deeply linked to the sign relation between t_z and M_z ; see Supplementary Text. Therefore, the sign relation suggested in Figs. 3 and 4 is limited to one specific chiral domain. However, the presence of the chiral domain is

not in conflict with our interpretation of the observed AHE, as it does not affect the measurement of σ_{xy} (see Supplementary Text for more explanations).

To summarize, a combination of triangular lattice, chirality, and coplanar 120° spin order gives rise to an interesting feature in $\text{Co}_{1/3}\text{TaS}_2$: the interplay between the field-tunable toroidal moment and AHE. We have shown that it exhibits large AHE from the vestige of symmetry-protected hourglass Weyl fermions, which has not been reported before. Moreover, $\text{Co}_{1/3}\text{TaS}_2$ reported in this work is a rare cleavable antiferromagnetic metal: we confirmed that $\text{Co}_{1/3}\text{TaS}_2$ could be exfoliated down to a few-nm thickness (Supplementary Figure 7). Therefore, it will further offer an exciting chance of studying noncollinear antiferromagnetism and relevant topological properties in a genuine two-dimensional limit, not to mention its rich bulk properties worth further studies.

Methods

Sample preparation and characterization. To obtain $\text{Co}_{1/3}\text{TaS}_2$ single crystals, we first synthesized polycrystalline $\text{Co}_{1/3}\text{TaS}_2$ using the solid-state reaction. A mixture of Co (Alfa Aesar, >99.99 %), Ta (Sigma Aldrich, >99.99%), and S (Sigma Aldrich, >99.999%) in a molar ratio of 1.15:3:6 was well ground in an Ar-filled glove box and sintered at 900 °C for 10 days in an evacuated quartz ampoule. We measured the powder X-ray diffraction using a commercial machine (Smartlab, Rigaku Japan) to find that it forms in the expected hexagonal structure of the $P6_322$ space group; the corresponding data are shown in Supplementary Figure 1 and Supplementary Table 1. We grew $\text{Co}_{1/3}\text{TaS}_2$ single-crystal starting with the pre-reacted powder by a chemical vapor transport technique in an evacuated quartz tube with I_2 as a transport agent ($4.5 \text{ mg I}_2/\text{cm}^3$). The quartz tube was placed in a two-zone furnace with a temperature gradient from 940 to 860 °C for 7~10 days. Finally, we obtained shiny hexagonal crystal pieces (4~13 mm) shown in Fig. 1a.

The obtained single crystals were examined by high-resolution single-crystal x-ray diffraction (XtaLAB PRO, Cu K_α , Rigaku Japan) and Raman spectroscopy (XperRam Compact, Nanobase Korea); see Supplementary Figure 2, 3, and Supplementary Table 2. These two measurements confirmed the high quality of our samples (see Supplementary Text for more details). We determined the Co composition (x in Co_xTaS_2) using both energy-dispersive X-ray (EDX) spectroscopy and inductively coupled plasma (ICP) spectroscopy (OPTIMA 8300, Perkin-Elmer USA). Both examinations allow us to give the exact value of x within a measurement error close to 1/3 (see Supplementary Table 3). Note that one can slightly tune the resultant stoichiometric ratio by changing excess Co in the starting mixture.

Bulk property measurements. Magnetic properties of $\text{Co}_{1/3}\text{TaS}_2$ were measured by the two commercial magnetometers (MPMS and PPMS-14 with the VSM option, Quantum Design USA). For the temperature-dependent weak ferromagnetic moment (Fig. 2e), we measured the magnetization of the field-cooled (9 T) sample from 2 to 80 K without a magnetic field. Specific heat of $\text{Co}_{1/3}\text{TaS}_2$ was measured by using the commercial setup (PPMS-14, Quantum design USA). The non-magnetic contribution to the specific heat was estimated by the summation of the Debye model and the electronic contribution linear with the temperature, where we used two Debye temperatures ($\theta_{D1}=270 \text{ K}$ and $\theta_{D2}=611.7 \text{ K}$) for the fitting due to the coexistence of heavy (Ta) and light (S) elements.

Longitudinal and Hall voltage of $\text{Co}_{1/3}\text{TaS}_2$ were measured by a standard four-probe method using our home-built cryostat, PPMS-9 (Quantum Design, USA), and Teslatron PT (Oxford, UK). All the samples used for the transport measurements were prepared in a straight rectangular shape with a uniform thickness. Hall resistivity data were antisymmetrized to remove any accidental longitudinal signal from the contact misalignment. To observe the temperature dependence of the anomalous Hall effect separated from the ordinary Hall effect (Fig. 2d), we measured the Hall voltage of the field-cooled ($\pm 9 \text{ T}$) sample from 2 to 80 K without a magnetic field. We removed the longitudinal component by antisymmetrizing the two datasets measured after the field cool under +9 T and -9 T, respectively.

Density functional theory (DFT) Calculations. First-principles calculations were carried out using ‘Vienna *ab initio* simulation package (VASP)³⁷⁻³⁹ based on projector augmented wave (PAW) potential⁴⁰ and within Perdew-Burke-Ernzerhof (PBE) type of GGA functional⁴¹. To properly take into account localized Co-3d orbitals, we adopted DFT+ U

method^{42,43} with the values of $U = 4.1$ eV and $J_{Hund} = 0.8$ eV as obtained by constrained RPA for CoO and Co⁴⁴. We used the Γ -centered k -grid of $6 \times 6 \times 4$ for the $\sqrt{3} \times \sqrt{3}$ magnetic supercell. The optimized crystal structure was used with the force criteria of 1 meV/Å. The plane-wave energy cutoff is 500 eV. The screw rotation eigenvalues of the Bloch bands were calculated using the ‘irvsp’⁴⁵. To investigate the topological properties of electronic states, we obtained Wannier functions using the ‘WANNIER90’ code⁴⁶. The Berry curvature and anomalous Hall conductivity were calculated using the ‘WannierTools’ package⁴⁷, using the following formula:

$$\Omega_{n,\alpha\beta} = 2 \operatorname{Im} \left(\left\langle \partial_{k_\alpha} u_{nk} \left| \partial_{k_\beta} u_{nk} \right. \right\rangle \right) \quad (2)$$

$$\sigma_{n,\alpha\beta} = \frac{e^2}{(2\pi)^2 h} \sum_n \int d\mathbf{k} f_n(\mathbf{k}) \Omega_{n,\alpha\beta}(\mathbf{k}), \quad (3)$$

where $\Omega_{n,\alpha\beta}$ is Berry curvature, $f_n(k)$ is the Fermi distribution function at 11.6 K, n is the band index, α and $\beta (\neq \alpha)$ denote the Cartesian coordinates (xyz), and u_{nk} is the periodic part of the Bloch function. We found it essential to take a dense-enough k -grid for accurately estimating the AHC value. After the convergence test, we adopted $301 \times 301 \times 301$.

Data Availability

The data used in this study are available from the corresponding author upon request.

Code Availability

Custom codes used in this article are available from the corresponding author upon request.

Acknowledgments

We acknowledge Dr. S. Lee, and Profs. K-Y Choi, C. Lee, and K. H. Kim for allowing us to use their instruments at the various stages of this work. This work was supported by the Samsung Science & Technology Foundation (Grant No. SSTF-BA2101-05). One of the authors (J.-G.P.) is partly funded by the Leading Researcher Program of the National Research Foundation of Korea (Grant No. 2020R1A3B2079375).

Author contributions

J.-G.P. initiated and supervised the project. P.P. grew the single crystals and performed all the bulk characterization. P.P. and J.K. measured the transport properties. J.K. performed the mechanical exfoliation and the characterization of the nanoflakes. Y.-G.K. and M.J.H. performed the DFT calculations. P.P., K.H.L., Y.-G.K., M.J.H., H.-J.N., and J.-G.P. contributed to the theoretical analysis and discussion. P.P. and J.-G.P. wrote the manuscript with contributions from all

authors.

Competing Interests

The authors declare no competing financial or non-financial interests.

Supplementary Information is available for this paper at [website url].

References

- 1 Bonbien, V. *et al.* Topological aspects of antiferromagnets. *J. Phys. D: Appl. Phys.* **55**, 103002 (2021).
- 2 Smejkal, L., MacDonald, A. H., Sinova, J., Nakatsuji, S. & Jungwirth, T. Anomalous Hall antiferromagnets. Preprint at <https://arxiv.org/abs/2107.03321> (2021).
- 3 Nagaosa, N., Sinova, J., Onoda, S., MacDonald, A. H. & Ong, N. P. Anomalous Hall effect. *Rev. Mod. Phys.* **82**, 1539-1592 (2010).
- 4 Taguchi, Y., Oohara, Y., Yoshizawa, H., Nagaosa, N. & Tokura, Y. Spin chirality, Berry phase, and anomalous Hall effect in a frustrated ferromagnet. *Science* **291**, 2573 (2001).
- 5 Chen, H., Niu, Q. & MacDonald, A. H. Anomalous Hall effect arising from noncollinear antiferromagnetism. *Phys. Rev. Lett.* **112**, 017205 (2014).
- 6 Kübler, J. & Felser, C. Non-collinear antiferromagnets and the anomalous Hall effect. *EPL (Europhys. Lett.)* **108**, 67001 (2014).
- 7 Nakatsuji, S., Kiyohara, N. & Higo, T. Large anomalous Hall effect in a non-collinear antiferromagnet at room temperature. *Nature* **527**, 212-215 (2015).
- 8 Nayak, A. K. *et al.* Large anomalous Hall effect driven by a nonvanishing Berry curvature in the noncolinear antiferromagnet Mn₃Ge. *Sci. Adv.* **2**, e1501870 (2016).
- 9 Kiyohara, N., Tomita, T. & Nakatsuji, S. Giant anomalous Hall effect in the chiral antiferromagnet Mn₃Ge. *Phys. Rev. Applied* **5**, 064009 (2016).
- 10 Suzuki, M. T., Koretsune, T., Ochi, M. & Arita, R. Cluster multipole theory for anomalous Hall effect in antiferromagnets. *Phys. Rev. B* **95**, 094406 (2017).
- 11 Suzuki, M. T. *et al.* Multipole expansion for magnetic structures: A generation scheme for a symmetry-adapted orthonormal basis set in the crystallographic point group. *Phys. Rev. B* **99**, 174407 (2019).
- 12 Higo, T. *et al.* Large magneto-optical Kerr effect and imaging of magnetic octupole domains in an antiferromagnetic metal. *Nat. Photonics* **12**, 73-78 (2018).
- 13 Spaldin, N. A., Fiebig, M. & Mostovoy, M. The toroidal moment in condensed-matter physics and its relation to the magnetoelectric effect. *J. Phys. Condens. Matter* **20**, 434203 (2008).
- 14 Parkin, S. S. P. & Friend, R. H. 3d transition-metal intercalates of the niobium and tantalum dichalcogenides. I. Magnetic properties. *Philos. Mag. B* **41**, 65-93 (1980).
- 15 Parkin, S. S. P. & Friend, R. H. 3d transition-metal intercalates of the niobium and tantalum dichalcogenides. II. Transport properties. *Philos. Mag. B* **41**, 95-112 (1980).
- 16 Lu, K. *et al.* Canted antiferromagnetic order in the monoaxial chiral magnets V_{1/3}TaS₂ and V_{1/3}NbS₂. *Phys. Rev. Mater.* **4**, 054416 (2020).
- 17 Parkin, S. S. P., Marseglia, E. A. & Brown, P. J. Magnetic structure of Co_{1/3}NbS₂ and Co_{1/3}TaS₂. *J. Phys. C: Solid State Phys.* **16**, 2765-2778 (1983).
- 18 Su, J. *et al.* Air-stable 2D intrinsic ferromagnetic Ta₃FeS₆ with four months durability. *Adv. Sci.* **7**, 2001722 (2020).
- 19 Fisher, M. E. The renormalization group in the theory of critical behavior. *Rev. Mod. Phys.* **46**, 597-616 (1974).
- 20 Kim, K.-S., Lee, K. H., Chung, S. B. & Park, J.-G. Magnon topology and thermal Hall effect in trimerized triangular lattice antiferromagnet. *Phys. Rev. B* **100**, 064412 (2019).
- 21 Munoz, A. *et al.* Magnetic structure of hexagonal RMnO₃ (R= Y, Sc): Thermal evolution from neutron powder diffraction data. *Phys. Rev. B* **62**, 9498 (2000).
- 22 Sim, H., Oh, J., Jeong, J., Le, M. D. & Park, J.-G. Hexagonal RMnO₃: a model system for two-dimensional triangular lattice antiferromagnets. *Acta Crystallogr. B: Struct. Sci. Cryst. Eng. Mater.* **72**, 3-19 (2016).
- 23 Ma, J. *et al.* Experimental evidence of hourglass fermion in the candidate nonsymmorphic topological insulator KHgSb. *Sci. Adv.* **3**, e1602415 (2017).
- 24 Wang, Z., Alexandradinata, A., Cava, R. J. & Bernevig, B. A. Hourglass fermions. *Nature* **532**, 189-194 (2016).
- 25 Zhang, J. *et al.* Topological band crossings in hexagonal materials. *Phys. Rev. Mater.* **2**, 074201 (2018).
- 26 Ezawa, M. Hourglass fermion surface states in stacked topological insulators with nonsymmorphic symmetry. *Phys. Rev. B* **94**, 155148 (2016).

- 27 Jiang, W., Huang, H., Liu, F., Wang, J.-P. & Low, T. Magnetic Weyl semimetals with diamond structure realized in spinel compounds. *Phys. Rev. B* **101**, 121113 (2020).
- 28 Zhang, H. *et al.* Three-dimensional Weyl hourglass networks in the nonsymmorphic half-metal Mg_2VO_4 . *Phys. Rev. B* **102**, 155116 (2020).
- 29 He, T. *et al.* Coexistence of fully spin-polarized Weyl nodal loop, nodal surface, and Dirac point in a family of quasi-one-dimensional half-metals. *Phys. Rev. B* **103**, 085135 (2021).
- 30 Zeng, Y., Wang, L. & Yao, D.-X. n-hourglass Weyl fermions in nonsymmorphic materials. *Phys. Rev. B* **101**, 115110 (2020).
- 31 Nielsen, H. B. & Ninomiya, M. Absence of neutrinos on a lattice: (I). Proof by homotopy theory. *Nucl. Phys. B* **185**, 20-40 (1981).
- 32 Ding, L. *et al.* Field-tunable toroidal moment in a chiral-lattice magnet. *Nat. Commun.* **12**, 5339 (2021).
- 33 Cheong, S.-W. SOS: symmetry-operational similarity. *npj Quantum Mater.* **4**, 53 (2019).
- 34 Cheong, S.-W., Lim, S., Du, K. & Huang, F.-T. Permutable SOS (symmetry operational similarity). *npj Quantum Mater.* **6**, 58 (2021).
- 35 Horibe, Y. *et al.* Color theorems, chiral domain topology, and magnetic properties of Fe_xTaS_2 . *J. Am. Chem. Soc.* **136**, 8368-8373 (2014).
- 36 Du, K. *et al.* Topological spin/structure couplings in layered chiral magnet $\text{Cr}_{1/3}\text{TaS}_2$: The discovery of spiral magnetic superstructure. *Proc. Natl. Acad. Sci.* **118** (2021).
- 37 Kresse, G. & Hafner, J. Ab initio molecular dynamics for open-shell transition metals. *Phys. Rev. B* **48**, 13115-13118 (1993).
- 38 Kresse, G. & Furthmüller, J. Efficient iterative schemes for ab initio total-energy calculations using a plane-wave basis set. *Phys. Rev. B* **54**, 11169-11186 (1996).
- 39 Kresse, G. & Furthmüller, J. Efficiency of ab-initio total energy calculations for metals and semiconductors using a plane-wave basis set. *Comput. Mater. Sci.* **6**, 15-50 (1996).
- 40 Kresse, G. & Joubert, D. From ultrasoft pseudopotentials to the projector augmented-wave method. *Phys. Rev. B* **59**, 1758-1775 (1999).
- 41 Perdew, J. P., Burke, K. & Ernzerhof, M. Generalized gradient approximation made simple. *Phys. Rev. Lett.* **77**, 3865-3868 (1996).
- 42 Anisimov, V. I., Zaanen, J. & Andersen, O. K. Band theory and Mott insulators: Hubbard U instead of Stoner I. *Phys. Rev. B* **44**, 943-954 (1991).
- 43 Liechtenstein, A. I., Anisimov, V. I. & Zaanen, J. Density-functional theory and strong interactions: Orbital ordering in Mott-Hubbard insulators. *Phys. Rev. B* **52**, R5467-R5470 (1995).
- 44 Sakuma, R. & Aryasetiawan, F. First-principles calculations of dynamical screened interactions for the transition metal oxides MO (M=Mn, Fe, Co, Ni). *Phys. Rev. B* **87**, 165118 (2013).
- 45 Gao, J., Wu, Q., Persson, C. & Wang, Z. Irvsp: To obtain irreducible representations of electronic states in the VASP. *Comput. Phys. Commun.* **261**, 107760 (2021).
- 46 Pizzi, G. *et al.* Wannier90 as a community code: new features and applications. *J. Phys. Condens. Matter* **32**, 165902 (2020).
- 47 Wu, Q., Zhang, S., Song, H.-F., Troyer, M. & Soluyanov, A. A. WannierTools: An open-source software package for novel topological materials. *Comput. Phys. Commun.* **224**, 405-416 (2018).

Figures

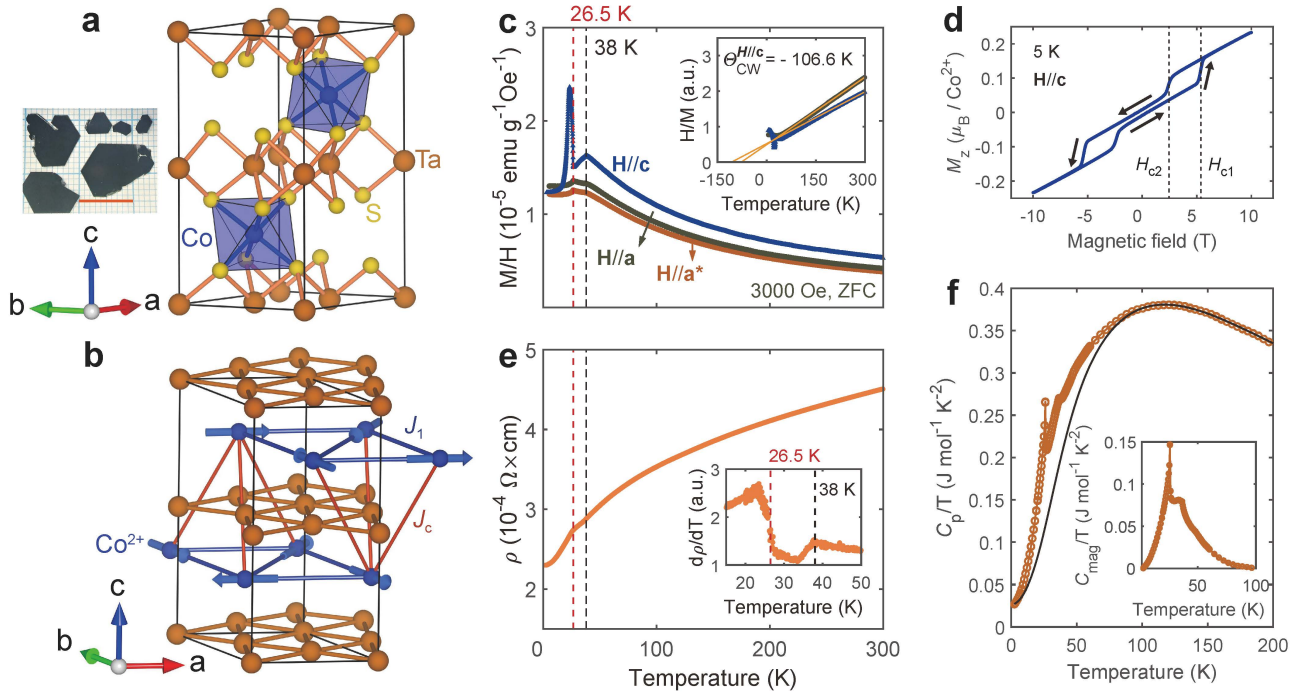


Fig. 1 | Structure and bulk properties of noncollinear metallic triangular antiferromagnet $\text{Co}_{1/3}\text{TaS}_2$. **a**, A crystallographic unit cell of $\text{Co}_{1/3}\text{TaS}_2$, where Co atoms are intercalated into octahedral sites. The image shows $\text{Co}_{1/3}\text{TaS}_2$ single crystals with the solid orange line as long as 10 mm. **b**, Noncollinear magnetic order (Γ_2) formed by magnetic moments of divalent Co ions. **c**, The magnetization of $\text{Co}_{1/3}\text{TaS}_2$ as a function of temperature along the three crystallographic axes. The inset shows the Curie-Weiss behavior of $\text{Co}_{1/3}\text{TaS}_2$. **d**, The field dependence of the magnetization along the c-axis at 5 K. In addition to apparent hysteresis from weak ferromagnetic domains ($\pm H_{c1}$), there is a jump of magnetization at $\pm H_{c2}$. **e**, Temperature-dependent resistivity of $\text{Co}_{1/3}\text{TaS}_2$ where its first derivative (inset) demonstrates two phase transitions, consistent with the magnetization data. **f**, Specific heat of $\text{Co}_{1/3}\text{TaS}_2$ as a function of temperature. The inset shows the specific heat after subtracting the non-magnetic contribution (see Methods).

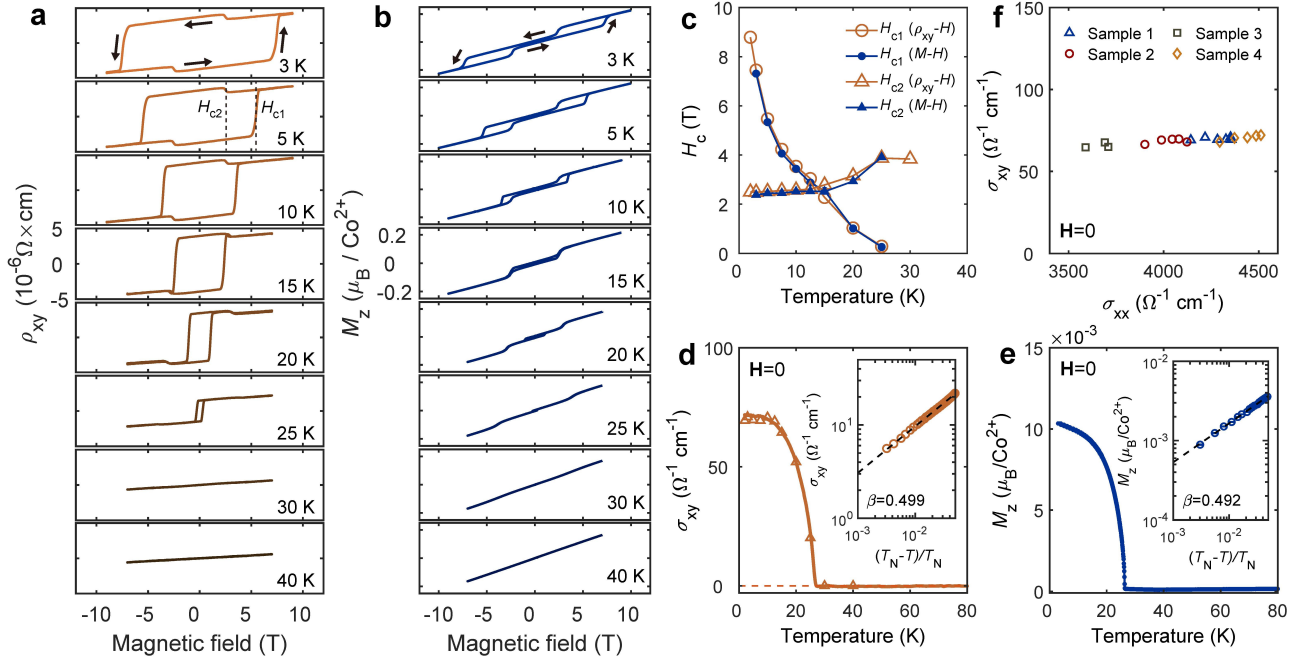


Fig. 2 | Anomalous Hall effect and its comparison to weak ferromagnetism. **a-b**, The field dependence of Hall resistivity ρ_{xy} and magnetization along the c-axis at several temperatures. **c**, Temperature dependence of H_{c1} (circles) and H_{c2} (triangles) determined from the $\rho_{xy}(\mathbf{H})$ (hollow symbols) and $M_z(\mathbf{H})$ (filled symbols) curves. **d-e**, Temperature-dependent zero-field Hall conductivity ($\sigma_{xy}(\mathbf{H} = 0)$) and zero-field magnetization along the c-axis ($M_z(\mathbf{H} = 0)$), measured after a field cooling process (see Methods). Inset shows the critical behavior of $\sigma_{xy}(T, \mathbf{H} = 0)$ and $M_z(T, \mathbf{H} = 0)$ near 26.5 K and fitted results (black dashed lines) with $\beta=0.499$ and 0.492, respectively. **f**, A plot of the longitudinal and zero-field anomalous Hall conductivity for several Co_xTaS_2 samples ($0.31 < x < 0.325$, see Supplementary Figure 6), which were extracted from the $\rho_{xy}(\mathbf{H})$ curves measured below 15 K.

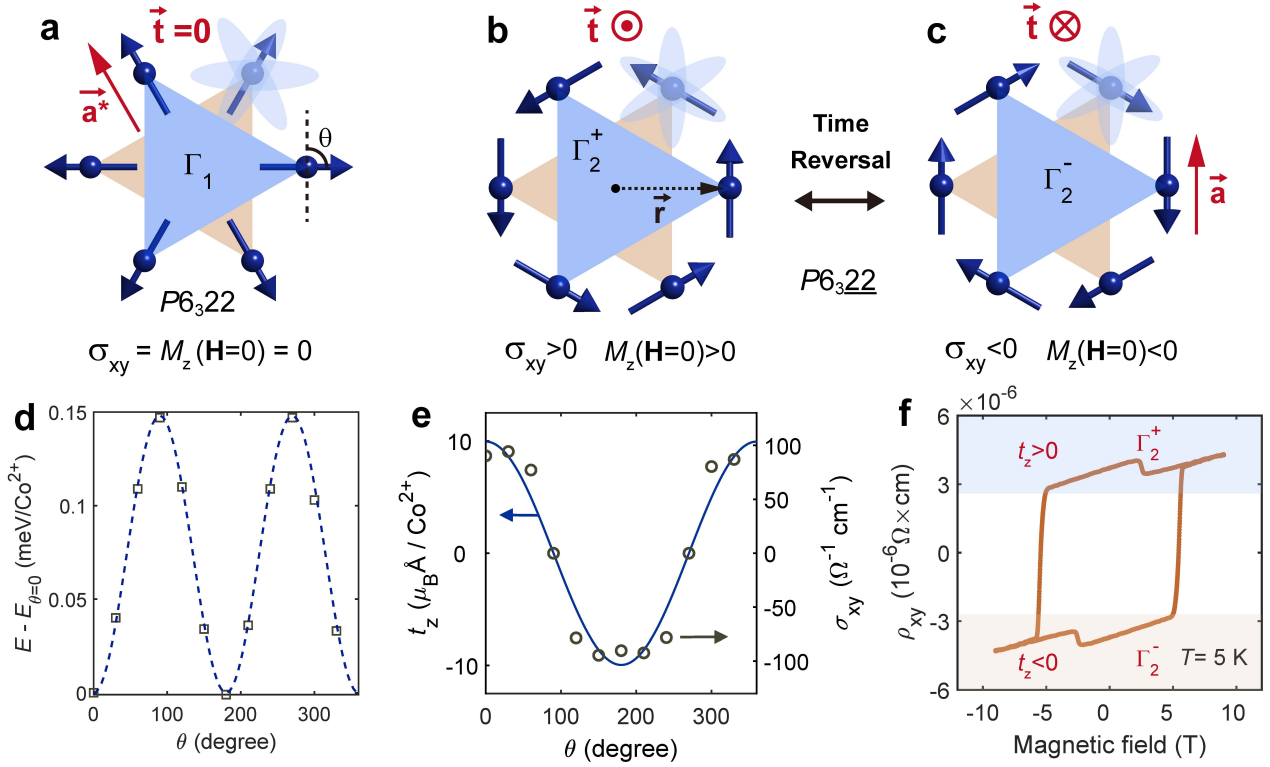


Fig. 3 | Interplay between a field-tunable toroidal moment and AHE. **a**, The Γ_1 spin configuration having a magnetic space group $P6_322$, in which the symmetry forbids finite $\sigma_{xy}(\mathbf{H} = 0)$ and $M_z(\mathbf{H} = 0)$. **b-c**, The Γ_2 spin configuration having a magnetic space group $P6_322$. No symmetry operation forces σ_{xy} and M_z to vanish. Three sky-blue ellipses in **a** and **b** denote the three-fold easy-axes to realize the Γ_1 or Γ_2 ground state, respectively. **d**, Total energy from the DFT calculation as a function of the uniform spin rotation angle θ shown in **a**. **e**, Comparison between a toroidal moment along the c-axis (a solid blue line) and calculated σ_{xy} for the spin configurations specified by θ in **a** (black circles). **f**, Interpreting the sign change of AHE as a switch of the toroidal moment. A blue (orange) rectangle denotes a region of the Γ_2^+ (Γ_2^-) spin configuration.

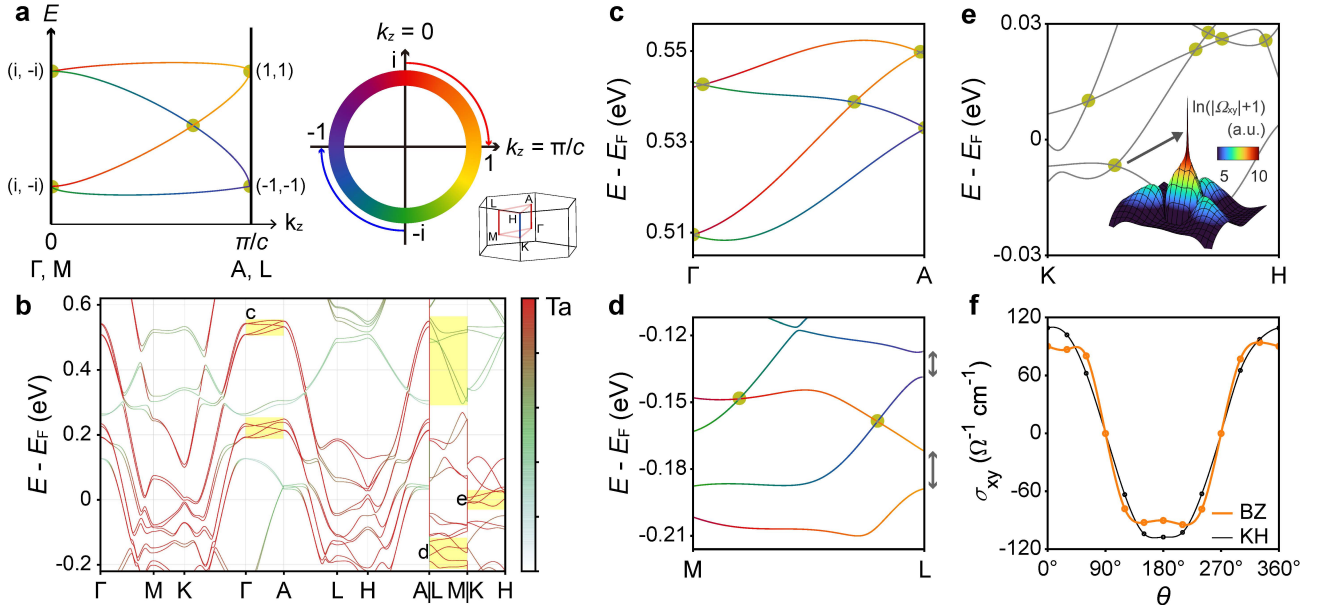


Fig. 4 | Hourglass Weyl dispersion with noncollinear magnetic order. **a**, A schematic band connectivity diagram for a screw-invariant line. The color scale indicates the 2_1 screw rotation eigenvalues of the Bloch bands. Kramers pairs with eigenvalues $(i, -i)$ are paired at $k_z = 0$ (Γ, M), and those with $(1, 1)$ or $(-1, -1)$ are paired at $k_z = \pi/c$ (A, L). The olive circles represent the Weyl point. The lower right figure shows the Brillouin zone of $\text{Co}_{1/3}\text{TaS}_2$ with high symmetry points being marked. **b**, The calculated band structure of the Γ_2^+ spin configuration of $\text{Co}_{1/3}\text{TaS}_2$. The Ta-5d portions are depicted by color code. Fermi level is set to zero energy. The yellow-colored regions correspond to the hourglass Weyl dispersion, some of which are enlarged in **c**, **d**, and **e**. **c-e**, The calculated band structure along the $\overline{\Gamma A}$, \overline{ML} and \overline{KH} lines, respectively (some of the yellow regions in **b**). Due to the broken TRS, the band degeneracy at the TRIM points is lifted. The color plot in **e** displays the calculated Berry curvature $|\Omega_{xy}|$ near the Weyl point designated by an arrow in a logarithmic scale. **f**, The calculated AHC by integrating over the whole Brillouin zone (BZ) (orange color) and only around the \overline{KH} line (black), respectively. θ denotes the angle of uniform spin rotation around the c-axis; see Fig. 3a.